NANO · MICRO small
www.small-journal.com

Engineering Structural Janus MXene-nanofibrils Aerogels for Season-Adaptive Radiative Thermal Regulation

Weiqing Yang, Peng Xiao, Shan Li, Feng Deng, Feng Ni, Chang Zhang, Jincui Gu, Jinlin Yang, Shiao-Wei Kuo, Fengxia Geng,* and Tao Chen**

Aerogels have provided a significant platform for passive radiation-enabled thermal regulation, arousing extensive interest due to their capabilities of radiative cooling or heating. However, there still remains challenge of developing functionally integrated aerogels for sustainable thermal regulation in both hot and cold environment. Here, Janus structured MXene-nanofibrils aerogel (JMNA) is rationally designed via a facile and efficient way. The achieved aerogel presents the characteristic of high porosity (≈98.2%), good mechanical strength (tensile stress of ≈2 MPa, compressive stress of ≈115 kPa), and macroscopic shaping property. Based on the asymmetric structure, the JMNA with switchable functional layers can alternatively enable passive radiative heating and cooling in winter and summer, respectively. As a proof of concept, JMNA can function as a switchable thermal-regulated roof to effectively enable the inner house model to maintain >25 °C in winter and <30 °C in hot summer. This design of Janus structured aerogels with compatible and expandable capabilities is promising to widely benefit the low-energy thermal regulation in changeable climate.

1. Introduction

In the 21st century, explosive growth of population has severely accelerated the energy consumption, which further leads to undesired energy crisis and even extreme weather.[1–3] Specifically, air-conditioning-based space cooling and heating, such as buildings and automobiles, is one of the important parts of energy consumption, which accounts for ≈12% of global energy per year.[4,5] In developed countries, the value can raise to over 40% in the building systems.[6,7] Despite the conventional insulation materials and related heating-cooling equipment that have been conducted,[8] pursuing new thermally regulated materials and technologies with non/low-energy consumption is highly desired. Recently, passive radiative thermal regulation has emerged as a promising solution to alternatively achieve thermal regulation without need of excess power input.[9–14] Therefore, radiation regulation is considered as a direct, efficient, and promising candidate to absorb input sunlight and further to energy saving. The radiation regulation significantly depends on the physically/chemically modified and synthesized materials, rational structural design and effective functional coordination. In recent years, diverse radiation regulation materials have been significantly developed, such as the thermochromic materials,[15–19] the electrochromic materials,[20,21] and mechanoresponsive materials.[22–25] However, the materials requirements of biocompatibility and multi-functionality are highly desired. Meanwhile, the complex preparation process and multi-layered structural design also limit the development of radiation regulation materials and their application. To this end, the rational design and fabrication of thermal regulated materials are crucial, which can remarkably improve the cooling or heating performance through adjustable physical or chemical structures.[26–28]

W. Yang, P. Xiao, S. Li, F. Deng, F. Ni, C. Zhang, J. Gu, T. Chen
Key Laboratory of Marine Materials and Related Technologies
Zhejiang Key Laboratory of Marine Materials
and Protective Technologies
Ningbo Institute of Materials Technology and Engineering
Chinese Academy of Sciences
Zhongguan West Road 1219, Ningbo 315201, China
E-mail: xiaopeng@nimte.ac.cn; tao.chen@nimte.ac.cn

W. Yang, P. Xiao, S. Li, F. Deng, F. Ni, C. Zhang, J. Gu, T. Chen
School of Chemical Sciences
University of Chinese Academy of Sciences
19A Yuquan Road, Beijing 100049, China

The ORCID identification number(s) for the author(s) of this article can be found under https://doi.org/10.1002/smll.202302509.

DOI: 10.1002/smll.202302509

J. Yang
State Key Laboratory of Marine Resource Utilization in South China Sea
Hainan University
Haikou 570228, China

S.-W. Kuo
Department of Material and Optoelectronic Science
Center of Crystal Research
National Sun Yat-Sen University
Kaohsiung 804, Taiwan

F. Geng
College of Energy
Soochow Institute for Energy and Materials Innovations (SIEMIS)
Key Laboratory of Advanced Carbon Materials and Wearable Energy
Technologies of Jiangsu Province
Soochow University
Suzhou 215006, China
E-mail: gengfx@suda.edu.cn

To achieve this objective, significant efforts have been devoted to exploit a series of developed materials systems, such as wood, aerogels, textiles, films, etc.[29–34] Among them, aerogels are characteristic of ultralightweight, highly porous, excellent optical properties, and large specific surface area,[35–37] which are expected to be promising materials for thermal regulation. Therefore, diverse aerogel materials have been developed for thermal management, including the MXene based aerogels,[38,39] Kevlar based nanofiber aerogels,[40,41] and Boron Nitride nanocomposite aerogels,[42,43] etc. However, some challenges still remain, including undesired mechanical brittleness, environmental unfriendliness, and poor climate adaptability.[44–46] Typically, conventional aerogels preparation was generally based on the freeze-drying method, resulting in limited sizes, weak mechanical strength, and also massive energy loss.[47–49] Moreover, when the climate changed, the achieved aerogels could scarcely adapt to the certain environment for alternative radiative cooling or heating.

In this work, we have designed a Janus-structured aerogels composed of photothermal MXene-CNF layer and CNF layer via a freeze-drying-free method, which enables switchable thermal regulation to integrate passive radiative cooling and heating into one material system for changeable environment. The achieved aerogels present good compressive strength (≈115 kPa), ultralow densities (4≈10 kg m^{-3}), and high porosity (≈98.2%). Based on the favorable mechanical properties, the Janus aerogel was employed as a smart roof for season-adaptive radiative thermal regulation. When CNF layer was exposed to the outer environment, the combination of outer layer high reflectivity and inner layer low infrared emissivity enabled an effective passive radiative cooling in summer. Furthermore, to tackle with the cold winter, the MXene-CNF layer was used as the outer layer, which could efficiently convert sunlight into considerable thermal energy. And the generated heat could be further transferred to the inner air through typical high infrared emissivity of CNF layer, resulting in a remarkable passive radiative heating. The facile fabrication method and rational design of Janus-structured aerogels provide an alternative pathway for the development of scalable climate-adaptive thermal regulated materials.

2. Results and Discussion

2.1. Application and Preparation Scheme of Janus MXene-Nanofibrils Aerogel

Ice-templating materials with well-defined microstructures play crucial roles in the fields of aerogels,[50,51] biomaterials,[52] catalysts,[53,54] separation,[55,56] and energy conversion.[57,58] Here, we prepared JMNA by ice templating method for season-adaptive radiative thermal regulation. The low infrared emissivity of the MXene-CNF layer enables further storage radiant energy and optimized cooling performance. The extremely high light absorption intensity of the MXene-CNF layer can absorb the solar energy and deliver it to the CNF layer with high infrared emissivity, thereby keeping indoor warm in winter through infrared thermal radiation (**Scheme 1**a). Meanwhile, the extremely high solar reflectivity and infrared emissivity of the CNF layer are beneficial to indoor radiative cooling in summer (Scheme 1b).

From Scheme 1c, JMNA were fabricated with the suspensions of CNFs, sodium alginate (SA), and MXene. For the JMNA system, in order to maintain a stable macroscopic morphology under the circumstance of materials transformation from hydrogels to aerogels, a strong, dense, and interconnected network is highly preferred. As shown in Figure S1a (Supporting Information), an ice templating strategy was employed. In this method, upon exposure of the hydrogels to temperatures below the freezing point, ice crystals nucleate and grow, resulting in the densification of the dispersed components in the progressively reducing volume between the ice crystals.[44] So, following thawing and solvent exchange, the CNF layer of JMNA has ice-templated pores (Figure 2a). Typically, a suspension of CNFs (0.4–1.4 wt.%) and SA was poured into a mold, followed by subjecting to freezing in a conventional freezer (≈-20 °C). The reciprocal negative charge of CNF and SA enables the formation of a homogeneous polymer mixture.[59] Meanwhile, with the introduction of sodium alginate and calcium ions, this technique can also produce water-resilient aerogels that do not collapse in water.[60–62] Moreover, interpenetrating polymeric network is formed, in which the CNF network is homogenously distributed within a Ca^{2+}-cross-linked network of sodium alginate to further improve JNA mechanical property. As shown in Figure S2 (Supporting Information), the compression performance of JNA without the addition of SA is about 20 kPa lower than that of JNA-SA. After pouring another solution of MXene (2 mg mL^{-1}) and CNFs to freezing, thawing, solvent exchange, and ambient drying (FTSA). The integration of the two layers was achieved by pre-freezing procedure, which enabled the formation of stable interface structure between the two layers. Therefore, JMNA was prepared by freeze-drying at ambient temperature (≈25 °C). Wet stability and mechanical strength can be obtained during post-dissolution during solvent exchange by incorporating $CaCO_3$ particles into the mixture. HCl and $CaCO_3$ release Ca^{2+} through chemical interaction during solvent exchange. Simultaneously, most of the carbonate ions were released from the system in the form of carbon dioxide. Furthermore, an interpenetrating polymeric network is then formed in which the CNF network is distributed within the Ca^{2+}-cross-linked network and intermolecular forces of SA and MXene. Meanwhile, cellulose abundant surface groups[49,63] (e.g., –COOH and –OH) ensured their affinity to MXene surfaces through interactions of van der Waals, coordination (e.g., fibril-C=O···Ti-MXene)[64] and H-bonding (e.g., fibril–OH···O–MXene, fibril–OH···F–MXene, and fibril–O···HO–MXene) (Figure S1b, Supporting Information).[49] In this way, the material to withstand the conversion from a hydrogel to an aerogel without collapsing, strong, wet-stable, and interconnected network is built, which is achieved in this work by ice templating and FTSA procedure. Season-adaptive radiative thermal regulation is also realized through differences in optical properties between the double layer of the JMNA.

2.2. Morphology and Physics Characterization of Janus MXene-Nanofibrils Aerogel

After the JMNA by dried at ambient temperature, the bilayer microstructure of the aerogel could be observed by SEM (**Figure 1**a;

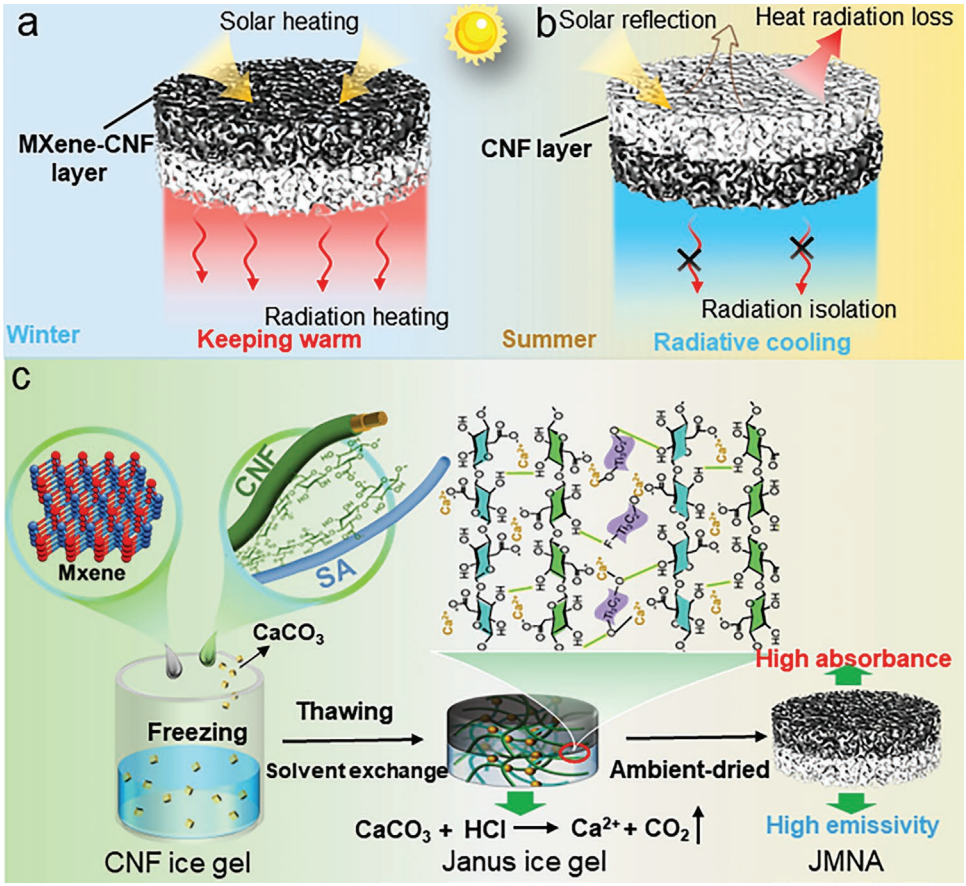

Scheme 1. JMNA application scheme for a) winter and b) summer thermal regulation. c) Preparation scheme of JMNA by ice templating method and FTSA procedure.

Figure S3, Supporting Information). From the SEM image of JMNA, we could find CNF layer with highly porous structure and MXene-CNF composite layer lamellar and wrinkled structure. For the Mxene-CNF layer, the morphology can be attributed to the 2D structure of MXene nanosheets. And the extrusion may be caused by the growth of ice crystals during freezing.[65] Meanwhile, the interface adhesion between the two layers is mainly achieved by hydrogen bonding and Ca^{2+}-cross-linking network. According to the Figure S5a (Supporting Information), the peel strength between MXene layer and CNF layer has been obtained with the value of ≈180 kPa through the two layers tensile stress test. In addition, we can also clearly observe the exfoliated MXene nano-lamellar structure from the TEM image of MXene (Figure S4, Supporting Information). In order to further optimize the properties of the JMNA, we optimize the CNF layer porosity, mechanical strength, and wet stability by adjusting the concentration of CNF. As shown in Figure 1b, the tensile stress of ambient-dried CNF aerogel (JNA) presented a gradually increasing tendency when the concentration of TEMPO-CNFs increased from 4 mg mL^{-1}, 6 mg mL^{-1}, 8 mg mL^{-1}, 10 mg mL^{-1}, 12 mg mL^{-1}, to 14 mg mL^{-1}. This is attributed to the increase in the CNF concentration, which enhanced the Ca^{2+}-cross-linked network. However, the excessive Ca^{2+}-cross-linked network could occupy numerous COO– on the cellulose nanofibers, which can severely lose hydrophilic groups of the cellulose nanofibers' surface, thus bringing a decline in water absorption and porosity (Figure 1c and Figure S6, Supporting Information). Therefore, the most suitable concentration of the TEMPO-CNFs was ≈10 mg mL^{-1} through the consideration of tensile stress, porosity, and water absorption performance. Thus, the JNA could be optimized with the porosity of ≈98.2%, the tensile stress of ≈2.2 MPa, and the water absorption of ≈60 g g^{-1} (Figure 1b,c) (see experimental section for the details about the porosity measurement). Also, as shown in Figure S5b (Supporting Information), the optimized JMNA tensile stress is ≈2 MPa. Furthermore, when the compressed aerogel absorbs water, these aerogels could also have excellent compression recovery performance (Figure 1d,e). From the Figure S7 (Supporting Information), when the JNA has no water absorption, it cannot be recovered after compression, and the increase of $CaCO_3$ will further improve the compression performance due to the strengthening of the Ca^{2+}-cross-linked network. Meanwhile, when the $CaCO_3$ content is more than 0.1 wt.%, the Ca^{2+} content is greater than that of the carboxyl groups, resulting in no redundant cross-linking sites left for Ca^{2+} cross-linking, and the mechanical properties of JNA have not been improved. Therefore, the $CaCO_3$ with the content of 0.1 wt.% in JNA system was alternatively selected for subsequent experiments and applications. However, JNA also exhibit remarkable wet shape-recovery after water absorption,

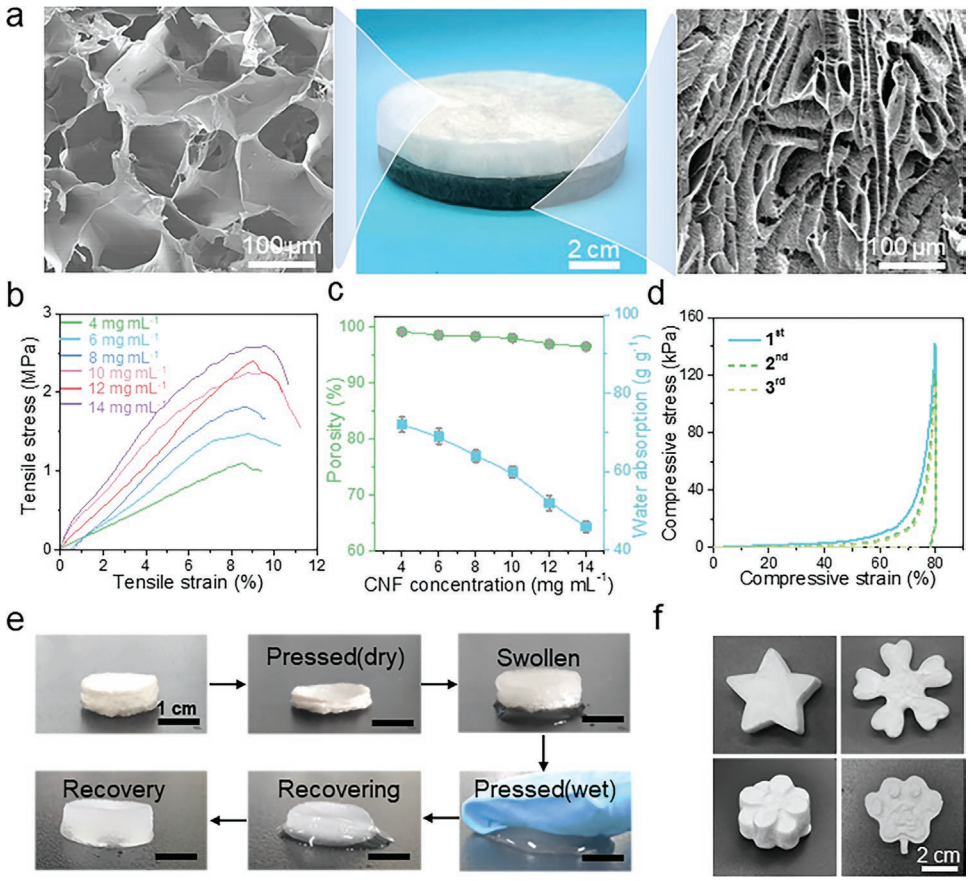

Figure 1. a) Electron micrographs of JMNA porous structure (CNF layer) and wrinkled structure (MXene-CNF layer) (the sample size: d = 10 cm, h = 2.5 cm). b) Tensile stress, c) porosity, water absorption properties, and d) cyclic (3 cycles) compression for JNA. e) Sequence of photographs showing the ability of wet JMNA to be compressed at 25 °C, and then re-wetted to regain its original dimensions (the sample size: d = 2 cm, h = 0.8 cm, test number: n = 3). f) Preparation of JNA in diverse shapes (the sample size: d = 5 cm, h = 2 cm, test number: n = 3).

followed by re-wetting (Figure 1e; Movie S1, Supporting Information). In addition, the JNA and JMNA have excellent cycle stability performance. As shown in Figure 1d and S5c (Supporting Information), the compressive stress remains ≈150 and ≈115 KPa after three-cycle compression, and the JNA recovery rate is ≈100% after repeated compression (Movie S2, Supporting Information), showing an excellent mechanical property of the JNMA. This excellent shape recovery also facilitates efficient and environmentally friendly delivery of these types of lightweight materials (Figure S8, Supporting Information). Meanwhile, the excellent stability and Ca^{2+}-cross-linked network of the JNA were also crucial for further applications of diverse shapes (Figure 1f; Figure S9, Supporting Information).

2.3. Thermal Regulation Mechanisms and Performance Evaluation

More importantly, the optimized concentration of CNF layer was combined with MXene to prepare JMNA for thermal regulation application. As shown in **Figure 2**b,d, the thermal regulation model is a smart window concept of JMNA, which is capable of high efficiency and continuous thermal regulation under sunlight illumination. Therefore, it can potentially be acted as a window screening bilayer aerogel of a temperature-manageable window. Thus, JMNA was expected to regulate the indoor temperature of living spaces suitable for human comfort. In winter, the MXene-CNF side of the window was exposed to sunlight, harvesting solar energy with the high solar absorption (≈97.5%) (Figure 2a). The absorbed solar energy was delivered to the CNF layer with high infrared emissivity, so the indoor temperature was raised by infrared thermal radiation. (Figure 2b,c). In summer, the CNF side was exposed to sunlight, reflecting solar energy with low absorption (≈12%) and porous structure (Figures 1a and 2a). Meanwhile, the CNF layer dissipates solar energy through outwardly infrared radiation. The low infrared emissivity of the MXene-CNF layer further reduces the energy diffusion to the interior, resulting in lower indoor temperature (Figure 2c,d).

In addition, the season-adaptive radiative thermal regulation of the JMNA also benefits from the difference in thermal conductivity between the MXene-CNF layer and the CNF layer.

Aerogels generally have ultralow thermal conductivities due to their highly porous three-dimensional network with nanopores. The thermal conductivity of the CNF layer is extremely low $\lambda \approx 0.025$ W m^{-1} k^{-1}, and the thermal conductivity increases with the increase of MXene, reaching $\lambda \approx 0.055$ W m^{-1} k^{-1} at a mass ratio of 3:1 (Figure 2f). Due to the high absorbance of

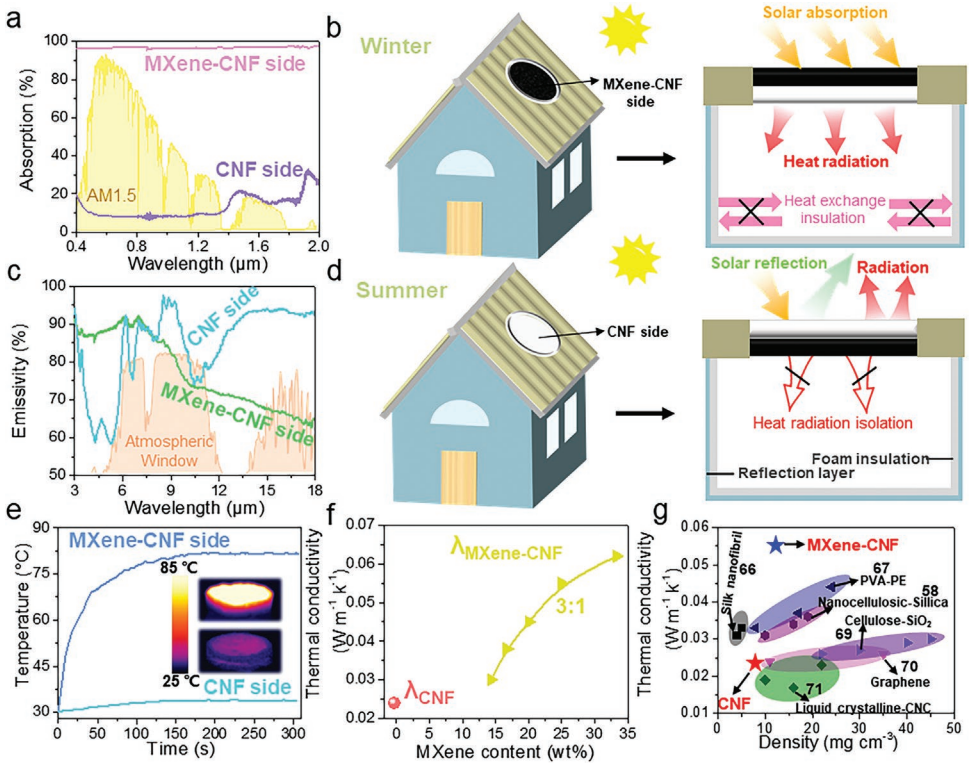

Figure 2. a) Absorption of MXene-CNF side and CNF side. b) Winter thermal regulation model (left) and heating mechanism (right). c) Infrared emissivity of the MXene-CNF side and CNF side. d) Summer thermal regulation model (left) and cooling mechanism (right). e) Surface temperature of MXene-CNF side and CNF side under one sun (the sample size: d = 5 cm, h = 2.5 cm, test number: $n = 3$). f) Thermal conductivity of CNF layer and MXene-CNF layer with different MXene contents (λ = W m^{-1} k^{-1}). g) Thermal conductivity comparing JMNA with relevant lightweight aerogel materials found in the literature.[66–71]

the MXene-CNF layer, the surface temperature can quickly reach 85 °C within 2 min in one sun, and the low absorbance and thermal conductivity of the CNF layer make the surface temperature only up ≈32 °C (Figure 2e). Furthermore, relatively speaking, considering other reported aerogel materials, the thermal conductivity of the CNF layer is lower than most aerogel materials and the MXene-CNF layer exhibited a superior overall performance as shown in Figure 2g.[66–71] Owing to the low thermal conductivity, the Janus aerogels with dynamic functional surfaces are expected to effectively realize the winter heating and summer cooling. Therefore, in specific environment of buildings, it is necessary to trap solar energy and transport it into the inner building in winter and block the solar energy into the inner building in summer. In winter, the CNF layer with low thermal conductivity is inside the building, which can remarkably decrease the building heat loss and heating loads. Also, in summer, the CNF layer at the outer surface can effectively block the thermal energy input and transport the absorbed the surface energy into the atmosphere via the high infrared emissivity.

In order to further demonstrate the thermal regulation mechanism of JMNA, indoor thermal regulation simulation experiments and structural optimization of JMNA were carried out. Inset of Figure S10 (Supporting Information) schematically illustrates the structure of the indoor experimental setup, and details can be found in the experimental section. Insulation foam and aluminum foil to isolate the heat exchange between the internal and external environment. The temperature of device inside was detected by thermal couple in different climatic conditions. The optimization of thermal regulation performance could be tuned by the thickness of the JMNA (**Figure 3**a; Figure S11, Supporting Information). In summer, we demonstrate that the combined effect of the absorbance and infrared emissivity of the JMNA could reduce the indoor temperature. Similarly, thicker JMNA can further optimize winter cooling by increasing solar reflection and transmission paths (Figure S12, Supporting Information). As shown in Figure S13a (Supporting Information), when the thickness of JMNA is thin in the range of 0.5–1 cm, which cannot remarkably affect the heat dissipation. However, the thermal convection is considered to contribute to the heat dissipation. Therefore, with the increase of the thickness, the temperature difference for winter heating can experience an improvement process. However, further increasing the thickness of JMNA ranging from 1 to 3 cm, the resulted heat transfer between the MXene-CNF layer and the CNF layer can be remarkably affected, resulting in the unfavourable increase of heat dissipation (Figure S13b, Supporting Information). In addition, the thickness ratio of the bilayer also played a significant role in the thermal regulation performance of the JMNA. If the MXene-CNF layer accounts for a large proportion, it is beneficent to the heating performance in winter (Figure S14, Supporting Information). Similarly, the CNF layer is dominant, it would be conducive the cooling performance in summer (Figure S15, Supporting

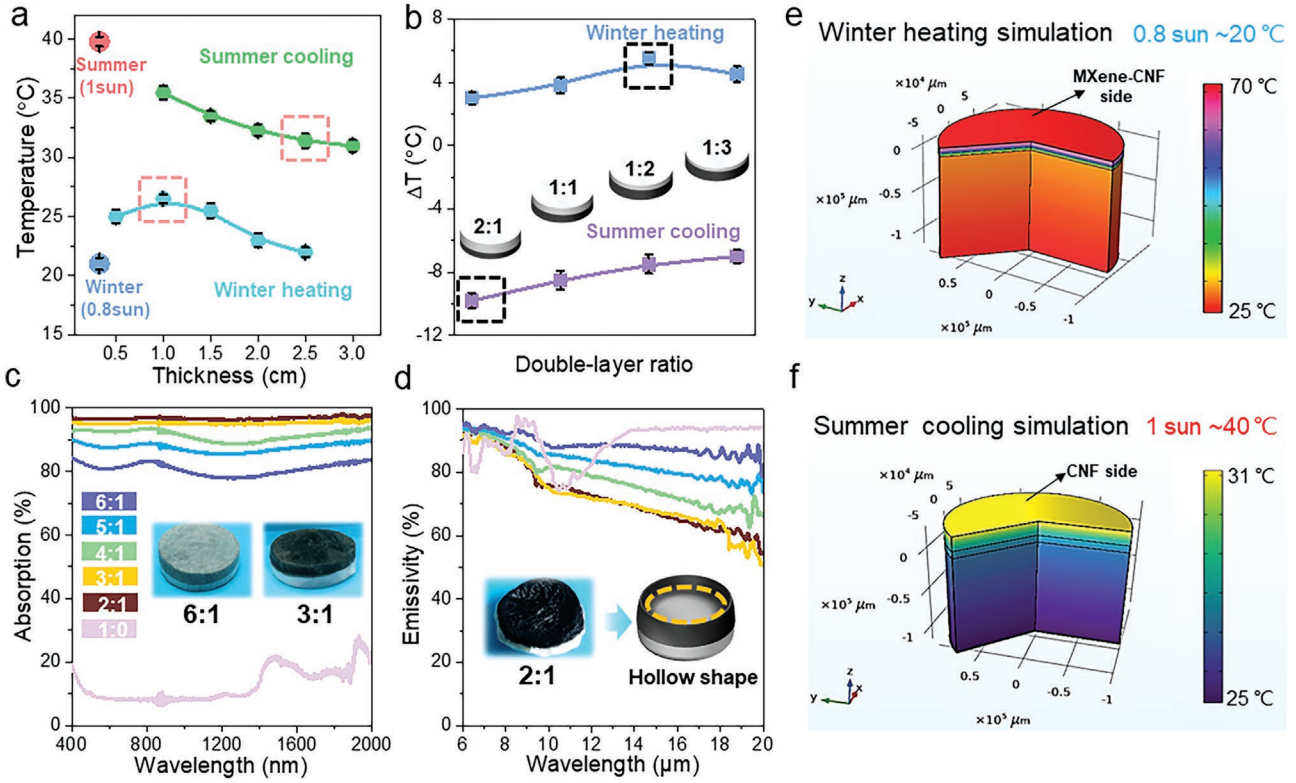

Figure 3. a) Indoor summer cooling and winter heating chamber interior temperature of JMNA with different thickness (1 sun = 1000 W m^{-2}, 0.8 sun = 800 W m^{-2}). b) Indoor summer cooling and winter heating chamber interior temperature difference of JMNA with different double-layer ratio. c) Absorption and d) infrared emissivity of MXene-CNF layer with different MXene contents (the sample size: d = 5 cm, h = 2.5 cm, test number: n = 3). COMSOL thermal regulation simulation of JMNA at e) winter heating and f) summer cooling.

Information). In general, when the bilayer thickness ratio of ≈1:2 and ≈2:1, the summer heating and winter cooling values of the JMNA reached the maximum ΔT at ≈5.5 °C and ≈–9.8 °C, respectively (Figure 3b).

More importantly, the MXene-CNF layer mass ratios of CNF and MXene also have a significant influence on the thermal regulation capability of the JMNA. As shown in Figure S16 (Supporting Information), the surface temperature of JMNA presented a gradually decreased tendency when the mass ratios of CNF and MXene increased from 2:1, 3:1, 4:1, 5:1,6:1, to 1:0. Moreover, there was a remarkable absorption and emissivity difference of MXene-CNF layer with the increased mass ratios of CNF and MXene (Figure 3c,d). Furthermore, the effect of the mass ratio of the JMNA bilayer on the thermal regulation performance was detected to receive an optimal mass ratio of MXene-CNF layer. When the relative proportion of MXene was high, the solar absorption showed a higher value and the emissivity showed a lower value (Figure 3c,d). So, we could know that a high proportion of MXene was beneficial to winter heating and summer cooling (Figures S17 and S18, Supporting Information). However, as shown in Figure 3d, the excessive MXene dispersions can reduce CNF content and Ca^{2+}-cross-linked network, which lead to the reduction in JMNA stability and severely affect the shape of JMNA. Besides, the thermal regulation may experience a declined performance (Figure 3d). Meanwhile, as shown in Figure S19a (Supporting Information), compared with the MXene films, the absorbance of MXene-CNF aerogel shows a higher value. To further explore the photothermal capacity, the temperature-time curve is displayed in Figure S19b (Supporting Information). It can be clearly observed that the temperature of the MXene-CNF aerogel is remarkably higher than that of the film under 1 sun irradiation. Therefore, Janus structured MXene-CNF aerogels are preferred in our system. Thus, considering benefits and thermal regulation performance, the JMNA could be optimized with the thickness of ≈2.5 cm (summer) and ≈1 cm (winter), the CNF and MXene mass ratios of ≈3:1, and the bilayer thickness ratio of ≈2:1 and ≈1:2 (Figure 3a,b; Figure S18, Supporting Information). Furthermore, with the increase of MXene concentration, the emissivity of the MXene-CNF side also could be decreased. As shown in Figure S20a (Supporting Information),b, the JMNA thermal emissivity of the MXene-CNF side presented a gradually decreaseing tendency as the MXene concentration increased from 2 mg mL^{-1}, 4 mg mL^{-1}, 6 mg mL^{-1}, to 8 mg mL^{-1}. It can be found that the emissivity is reduced from 75% to 52% in the infrared thermal band of the atmospheric window. Meanwhile, with the increase of MXene concentration, the MXene-CNF layer aerogels still maintained favourable mechanical strength (Figure S20c, Supporting Information). Therefore, the emissivity of the MXene-CNF side could be effectively adjusted by controlling MXene concentration. Based on the above-mentioned strategy, the emissivity of MXene-CNF side can be rationally controlled to be lower values. As a result, the heat loss in winter can be

effectively reduced with the improvement of radiative heating. Meanwhile, comparative experiments were conducted to testify the practical thermal regulation performance of JMNA. The summer cooling and winter heating performance were further compared with JNA in a window-closed room with continual changing of ambient temperatureand solar intensity (Figure S21, Supporting Information). The temperature difference (ΔT) and thermal regulation capacities of JMNA were higher than the CNF aerogel.

Apart from this, to further evaluate the cooling and warming capacities of the JMNA, we performed a COMSOL simulation heat transfer model to analyze the cooling and warming capability (Figure 3e,f). For the simulation in a cold environment, the JMNA surface temperature (T_s) was ≈70 °C and that of the ambient temperature was set to 20 °C in 0.8 sun; this range includes the temperature change of the JMNA and interior space (Figure 3e). Similarly, T_s was ≈31 °C and that of the ambient temperature was set to 40 °C in 1 sun to simulate a hot environment (Figure 3f). More detailed information on the simulation is presented in Figures S22–S24 (Supporting Information) in the Supporting Information. Parameter setting used in this study is depicted in Tables S1 and S2 (Supporting Information). Heat transfer mainly occurs in the Z-direction, and the grids are divided into multiple layers, and the grid can be appropriately coarsened. There is no air convection on the sides for heat dissipation. Originally, the winter heating simulation structure had a lower ambient temperatures of 20 °C. However, the T_s of the structure increased to ≈70 °C, which is attributed to the high absorbance of the MXene-CNF layer. Similarly, the T_s of the summer cooling structure ≈31 °C, which is attributed to the low absorbance and thermal conductivity of the CNF layer. Furthermore, the JMNA temperature contour images of the simulation are shown in Figure S22 (Supporting Information) for the JMNA bottom temperature of ≈28 and ≈29 °C in winter heating and summer cooling, respectively. The simulated results are approximately consistent with the experimental results, and the JMNA shows thermal regulation capacity in both summer and winter environments.

2.4. Outdoor Thermal Regulation Performance Testing and Analysis

Moreover, a practical application for the thermal regulation performance of the JMNA was carried out in the actual outdoor environment. The outdoor experimental application site is located on the roof terrace (urban area in Ningbo, 29.55° N, 121.37° E; subtropical monsoon climate). JMNA and CNF aerogel were placed next to each other and exposed to direct sunlight, as shown in **Figure 4**a. In winter, the MXene-CNF layer of JMNA in Figure 4a was horizontally faced to the sky. CNF aerogel was selected in the chamber as a control group to demonstrate the thermal regulation ability of the JMNA. Inset of Figure 4b schematically illustrates the structure inside the chamber and details about the experimental setup can be found in the experimental section. Thermocouples were encapsulated inside the PS foam chamber, and aerogel backs were well insulated. A solar radiometer was used to monitor the solar intensity. Chamber internal and ambient temperature was tracked by the thermocouple of multi-channel temperature tester and the temperature & humidity recorder. PMMA board were used to reduce the convection heating from ambient air, which is more in line with the practical application scenarios. As shown in Figure 4d, the average solar intensity was ≈0.72 Kw m^{-2} and the average relative humidity was ≈40% during the experimental period (Beijing time 10–15 o'clock, Ningbo in south China, Daytime on Dec. 3th, 2021). Figure 4e shows that the chamber temperature of JMNA is ≈6 °C higher than that of CNF aerogel and ≈4 °C higher than ambient temperature. The temperature tracking result (Figure 4c) and the distribution of temperature difference (Figure 4e) demonstrate the reliability of the real-time measurement systems compared with the lab experiment and thermal regulation simulations. These temperature differences illustrate the advantageous heating capability of the JMNA.

Similarly, in summer, the CNF layer of JMNA in **Figure 5**d was horizontally facing to the sky. We can know that the average solar intensity and relative humidity period were ≈0.8 kW m^{-2} and ≈42% during the experimental period (Beijing time 12:30–14:30, Ningbo in south China, daytime on October 8, 2021). Furthermore, as shown in Figure 5c, the chamber temperature of JMNA is ≈1.5 °C lower than that of CNF aerogel and ≈7 °C lower than ambient temperature. The temperature tracking result (Figure 5a) and the distribution of temperature difference (Figure 5c) demonstrate the advantageous cooling capability of the JMNA. Meanwhile, in 1 sun, the CNF layer surface temperature and temperature difference (ΔT) were further compared with other insulation aerogel or polymer materials. The CNF layer surface temperature and temperature difference (ΔT) of JMNA were lower than other insulation aerogel or polymer materials (Figures S25 and S26, Supporting Information).

Furthermore, JMNA and CNF aerogel volume shows a decrease of only ≈6% of their initial volume after 20 adsorption–desorption thermal regulation performance cycles (Figure 5e; Figure S27, Supporting Information) but reaches a steady state after 5 cycles. It can be observed that the results present a slight decrease of its volume from 9.8 cm^3 to 9.2 cm^3, which exhibits an excellent cycle stability. Therefore, due to the porous, Ca^{2+}-cross-linked network structure, and re-wetting stability, JMNA shows an excellent mechanical property, cycle stability and volume stability. This also improves the durability and tolerance of JMNA in practical thermal regulation applications. Meanwhile, the JMNA presented favorable thermal regulation, which was comparable to the majority of the previously reported non-biomass and other biomass materials in summer cooling (Figure 5f).[11,26,72–77] The high temperature regulation performance and stability of JMNA suggests that these materials pave the way towards the development of new highly efficient processes for season-adaptive radiative thermal regulation.

3. Conclusion

In summary, we have proposed a Janus-structured aerogel via a freeze-drying-free method for climate-adaptive passive radiative thermal regulation. In our system, the Janus MXene-nanofibrils

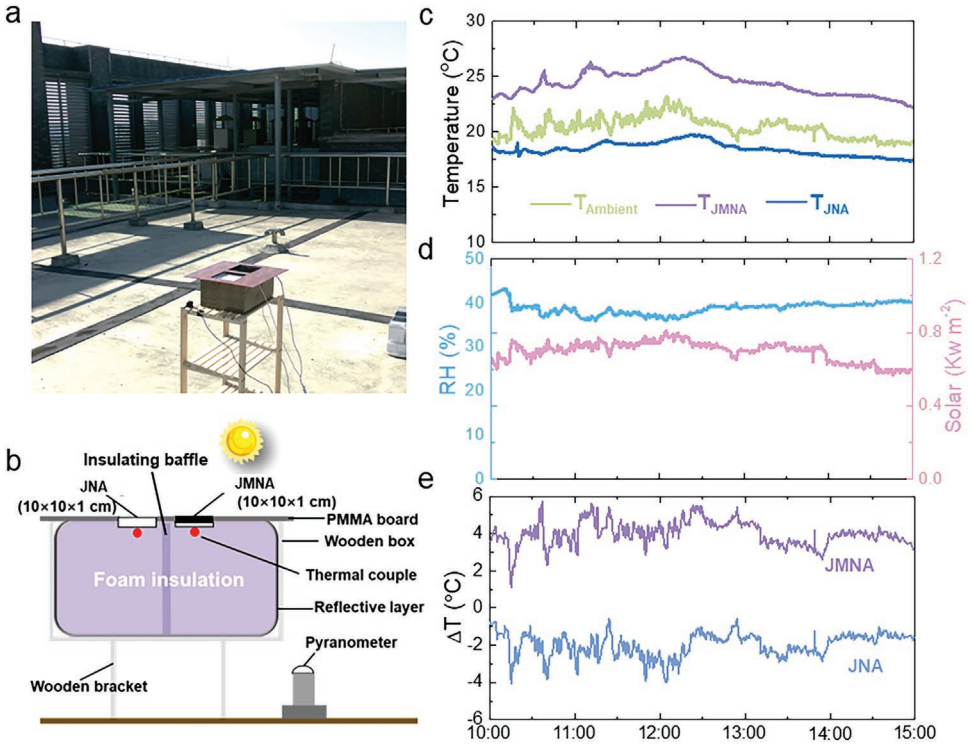

Figure 4. a) Photograph and b) schematic of the outdoor temperature measurement thermal regulation setup in winter environment (urban area in Ningbo, 29.55° N, 121.37° E, Dec 03, 2021) (the sample size: ≈10 cm ×10 cm×1 cm, test number: $n = 3$). c) Temperature tracking of the JMNA, JNA, and ambient air. d) Solar intensity and relative humidity variations. e) JMNA and JNA temperature difference variations relative to ambient temperature. (Time: 10:30–15:00.)

aerogel was effectively prepared via a facile freeze-drying-free method, demonstrating the characteristic of good mechanical strength, high porosity, and low density. The achieved Janus aerogel could function as a smart roof for both passive radiative cooling and heating through the switchable surface. Therefore, the Janus aerogel with CNF layer exposed to the outer space can result in high reflection and low absorbance of sunlight, but low infrared emissivity into inner house. On the contrary, when the MXene-CNF composite layer with high absorbance and low infrared emissivity was used as the outer layer, the Janus one could effectively convert sunlight into considerable thermal energy and the inner CNF layer could prominently elevate the inner temperature through high infrared emissivity. As a result, the indoor temperature could maintain below 30 °C in summer with ambient temperature of ≈40 °C, and >25 °C in winter with ambient temperature of ≈20 °C.

4. Experimental Section

Materials: TEMPO-CNFs were purchased from Zhejiang Jinjiahao Green Nano Material Co., Ltd. MXene were purchased from Science Compass-Feynman Nano. Sodium Alginate and $CaCO_3$ were produced by Shanghai Aladdin Biochemical Technology Co., Ltd. Acetone and HCl were purchased from Sinopharm Chemical Reagent Co., Ltd.

Preparation of Ambient-Dried Ca^{2+}-Cross-Linked Network CNF Aerogels: TEMPO-CNFs (1.0 wt.%) and alginate solution (0.5 wt.%) were mixed in a mass ratio of 40:1. The $CaCO_3$ particle suspension (0.1 wt.%) was then added to the CNF-SA mixture. The mixture is stirred for 1–2 h, and then evenly distributed into polystyrene petri dishes (20 mm wide and 10 mm high). The mold was kept in the fridge (4 °C, 1 h) to homogenize the temperature within the dishes before freezing overnight (–20 °C). The following day, the frozen hydrogel was put in a solution of hydrochloric acid (0.1 mol) in acetone for 1 h at room temperature before being solvent exchanged with pure acetone (3×30 min). The acetone-soaked aerogels were subsequently ambient-dried. Finally, the ambient-dried CNF aerogel was successfully prepared.

Preparation of Ambient-Dried Janus MXene-nanofibrils Aerogels: TEMPO-CNFs (1.0 wt.%) and alginate solution (0.5 wt.%) were mixed in a mass ratio of 40:1. The $CaCO_3$ particle suspension (0.1 wt.%) was then added to the CNF-SA mixture. Similarly, another mixture with a mass ratio of TEMPO-CNF(1.0 wt.%) and MXene (0.2 wt.%) of 3:1 was mixed. The $CaCO_3$ particle suspension (0.1 wt.%) was then added to the CNF-MXene mixture. These two mixtures were stirred for 1–2 h, and then evenly distributed into two polystyrene petri dishes (20 mm wide and 10 mm high), respectively. The molds were kept in the fridge (4 °C, 1 h) to homogenize the temperature within the dishes. Furthermore, the suspension of CNF-SA-$CaCO_3$ mixture was followed by subjecting to freezing (–20 °C). Freezing was also performed after pouring another solution of CNF-MXene-$CaCO_3$ mixture (–20 °C). The following day, the Janus frozen hydrogel was put in a solution of hydrochloric acid (0.1 mol) in acetone for 1 h at room temperature before being solvent exchanged with pure acetone (3×30 min). The acetone-soaked aerogels were subsequently ambient-dried. Finally, the ambient-dried Janus MXene- nanofibrils aerogel was successfully prepared.

Porosity Calculation and Measurement of Ca^{2+}-Cross-Linked Network CNF Aerogel: The CNF aerogel porosity (θ) is expressed as:

$$\theta = \frac{\rho_c - \rho_a}{\rho_c} \times 100\% \quad (1)$$

The porosity was determined by the densities of the aerogel (ρ_a) and pure cellulose (ρ_c). $\rho_c$was set as ≈1.27 g cm^{-3}. ρ_a, is functions of aerogel mass (m_a) and volume (v_a), which is expressed as:

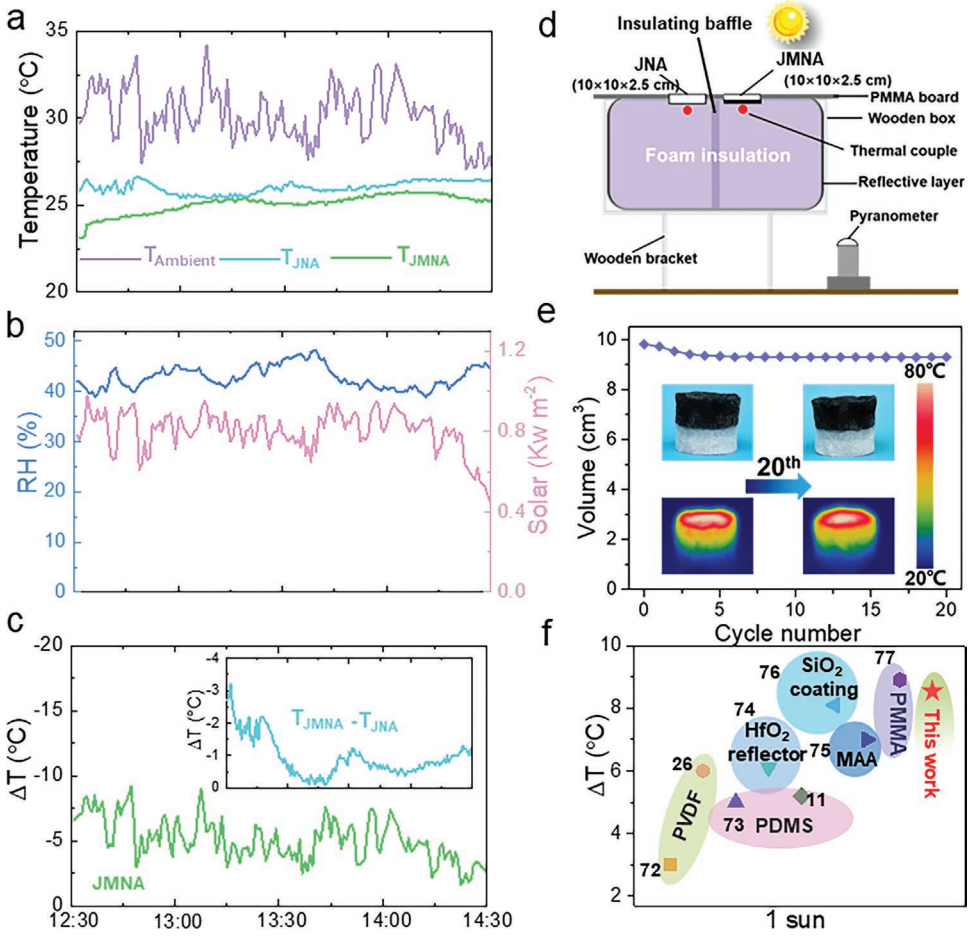

Figure 5. a) Temperature tracking of the JMNA, JNA, and ambient air. b) Solar intensity and relative humidity variations. c) JMNA temperature difference variations relative to ambient temperature and JNA temperature (illustration). (Time: 12:30–14:30). d) Schematic of the outdoor temperature measurement thermal regulation setup in summer environment (urban area in Ningbo, 29.55° N, 121.37° E, Oct 08, 2021). e) JMNA volume variations in cycling stability test and thermal imaging (the sample size: d = 2 cm, h = 2 cm, test number: $n = 20$). f) Cooling temperature difference comparing JMNA with relevant cooling and insulation materials found in the literature.[11,26,72–77]

$$\rho_a = \frac{m_a}{v_a} \tag{2}$$

Indoor Thermal Regulation Simulation Test: As shown in Figure S10 (Supporting Information), to initially investigate and optimize the thermal regulation performance of JMNA, "indoor experiments" were conducted by using a self-designed testing device. Similarly, used were thermal-insulated devices covered by aluminum foil in attempts to prevent the devices from being heated by reflecting solar light. To maintain the structural stability of the device, insulation foam was used as a framework inside and also to further insulate heat exchange between the internal and external environment. With high stability and strength, a 10 cm diameter JMNA was fixed and attached smoothly on the aluminum foil edge. Set different solar intensities and simulate harsh summer climates with a solar simulator. Meanwhile, simulate winter climatic environmental conditions with an indoor air conditioning system. A thermocouple was connected with a multi-channel temperature tester (JK-4000, China) to record the temperature of the sample inside and the bottom layer in real time.

Actual Outdoor Environment Thermal Regulation Test: As shown in Figures 4b and 5d, the insulating baffle consisted of insulating foam and rubber plastic cotton made of high-density butyl rubber, and the outermost aluminum foil was packaged in the surface of the wooden box to reduce heat conduction with the ambient environment. The top layer was a PMMA board to reduce convection. Each individual chamber was separated by insulating foam to reduce internal convection and conduction. In winter, the MXene-CNF layer is exposed on the outside, which increases the inside chamber temperature by absorbing solar energy and internal infrared thermal radiation. Similarly, in summer, the CNF layer is on the outside, which reduces the inside chamber temperature by reflecting sunlight and reducing thermal radiation. Meanwhile, the multi-channel temperature tester (JK-4000, China) detects the temperature in the two chambers. The ambient temperature and humidity were simultaneously recorded by a Temperature & Humidity recorder (Cos-03, China).

Thermal Regulation Measurement: The IR camera (FLIR E8, Germany) was employed to realize a real-time recording of the surface temperature and IR images of the different aerogel samples. For the outdoor thermal measurement, a self-designed device was used to conduct experimental tests under different conditions. The solar power was measured with a solar radiometer (TES-132, China).

COMSOL Thermal Regulation Simulation: Season-adaptive radiative thermal regulation simulation was completed by computer using COMSOL software. COMSOL multiphysics was a cross-platform finite element analysis and multiphysics simulation software. This software allowed conventional physics-based user interfaces and coupled systems of partial differential equations. The numerical simulations were

conducted by COMSOL multiphysics under steady analysis mode with a model built using a cartesian coordinate system. The physical properties of the aerogel and indoor space environment were measured in this work or were taken from the literature.[78] The mesh and parameter setting used in this study is depicted in Figures S22–S24 and Table S1 and S2 (Supporting Information).

Characterizations: Transmission electron microscopy (TEM, Japan) and field emission scanning electron microscopy (FESEM, Japan) images were performed on JEOL-2100-HR (JEOL, Japan) and Hitachi-S4800 (Hitachi, Japan), respectively. Ultraviolet–visible–near infrared (UV–vis–NIR) spectrophotometer (PerkinElmer, Lambda 950, USA) was used to test the transmittance and reflection of the aerogel samples. The IR reflectance and transmittance of the aerogel samples were measured with an FTIR spectrometer (NICOLET-6700, Thermo, USA) equipped with a diffuse gold integrating sphere. The solar simulator (PL-X300DF, China) was used to adjust the solar intensity. A universal tensile testing machine (Zwick, Z1.0, Germany) was used to characterize the tensile stress and compressive stress properties of the aerogel. Thermal conductivities of JMNA and JNA were tested by the laser thermal conductivity meter (LFA457, Germany).

Statistical Analysis: The experimental data of temperature – time curve was not pre-processed. The temperature at CNF side and MXene-CNF side were tested by thermocouple, and the error bars of experimental data were presented with a mean ± standard deviation (SD). The sample size for optical characterization was 10 cm × 2.5 cm (d × h). The experimental data of porosity, water absorption, and indoor simulation Test were tested at least three locations and presented with mean ± standard deviation. The software of Excel was employed to conduct one-way analysis of variance (one-way ANOVA), and the difference among samples was considered to be important when the calculated *p*-value was <0.05. Season-adaptive radiative thermal regulation simulation and analysis were completed by computer using COMSOL software.

Supporting Information

Supporting Information is available from the Wiley Online Library or from the author.

Acknowledgements

This research was supported by the Natural Science Foundation of China (52073295), Youth Innovation Promotion Association of Chinese Academy of Sciences (No.2023313), the Sino-German Mobility Program (M-0424), Ningbo Public Welfare Science and Technology Plan Project (2021S150), Ningbo Science and Technology Bureau (2021Z127), Key Research Program of Frontier Sciences, Chinese Academy of Sciences (QYZDB-SSWSLH036), Bureau of International Cooperation, Chinese Academy of Sciences (174433KYSB20170061), and K. C. Wong Education Foundation (GJTD-2019-13).

Conflict of Interest

The authors declare no conflict of interest.

Author Contributions

P.X. and W.Y. conceived the idea. W.Y. designed the experiments and performed the material preparation and characterization. W.Y. performed the modelling and the outdoor experiments work with the help of S.L., F.D., F.N., Z.C. and J. G., P.X., J.Y., S.K. helped with writing the manuscript. T.C. and F.G. supervised the project and provided financial support. All the authors provided discussion and comments.

Data Availability Statement

The data that support the findings of this study are available from the corresponding author upon reasonable request.

Keywords

biocompatible aerogels, cooling and heating, freeze-drying-free method, Janus structures, passive radiative, switchable functional surfaces

Received: March 24, 2023
Published online: April 7, 2023

[1] C. Lesk, P. Rowhani, N. Ramankutty, *Nature* **2016**, *529*, 84.
[2] P. Mathaios, M. Pierluigi, *Electr. Power Syst. Res.* **2015**, *127*, 259.
[3] L. Cai, A. Song, W. Li, P. Hsu, D. Lin, P. Catrysse, Y. Liu, Y. Peng, J. Chen, H. Wang, J. Xu, A. Yang, S. Fan, Y. Cui, *Adv. Mater.* **2018**, *30*, 1802152.
[4] A. Henry, R. Prasher, A. Majumdar, *Nat. Energy* **2020**, *5*, 635.
[5] M. Burke, S. Hsiang, E. Miguel, *Nature* **2015**, *527*, 235.
[6] Y. Ke, C. Zhou, Y. Zhou, S. Wang, S. Chan, Y. Long, *Adv. Funct. Mater.* **2018**, *28*, 1800113.
[7] L. Bell, *Science* **2008**, *321*, 1457.
[8] N. Shi, C. Tsai, F. Camino, G. Bernard, N. Yu, R. Wehner, *Science* **2015**, *349*, 298.
[9] S. Gong, X. Sheng, X. Li, M. Sheng, H. Wu, X. Lu, J. Qu, *Adv. Funct. Mater.* **2022**, 2200570.
[10] X. Xue, M. Qiu, Y. Li, Q. Zhang, S. Li, Z. Yang, C. Feng, W. Zhang, J. Dai, D. Lei, W. Jin, L. Xu, T. Zhang, J. Qin, H. Wang, S. Fan, *Adv. Mater.* **2020**, *32*, 1906751.
[11] L. Zhou, J. Rada, H. Zhang, H. Song, S. Mirniaharikandi, B. Ooi, Q. Gan, *Adv. Sci.* **2021**, *8*, 2102502.
[12] X. Zhang, W. Yang, Z. Shao, Y. Li, Y. Su, Q. Zhang, C. Hou, H. Wang, *ACS Nano* **2022**, *16*, 2188.
[13] L. Zhou, H. Song, J. Liang, M. Singer, M. Zhou, E. Stegenburgs, N. Zhang, C. Xu, T. Ng, Z. Yu, B. Ooi, Q. Gan, *Nat. Sustain.* **2019**, *2*, 718.
[14] Y. Fang, X. Zhao, G. Chen, T. Tat, J. Chen, *Joule* **2021**, *5*, 752.
[15] Y. Ke, Y. Yin, Q. Zhang, Y. Tan, P. Hu, S. Wang, Y. Tang, Y. Zhou, X. Wen, S. Wu, T. J. White, J. Yin, J. Peng, Q. Xiong, D. Zhao, Y. Long, *Joule* **2019**, *3*, 858.
[16] S. Liu, Y. Du, C. Y. Tso, H. H. Lee, R. Cheng, S. Feng, K. M. Yu, *Adv. Funct. Mater.* **2021**, *31*, 2010426.
[17] Y. Zhao, D. Fan, Q. Li, *Mater. Des.* **2022**, *219*, 110719.
[18] C. Lin, J. Hur, C. Y. H. Chao, G. Liu, S. Yao, W. Li, B. Huang, *Sci. Adv.* **2022**, *8*, eabn7359.
[19] Y. Zhou, S. Wang, J. Peng, Y. Tan, C. Li, F. Y. C. Boey, Y. Long, *Joule* **2020**, *4*, 2458.
[20] H. Gong, J. Ai, W. Li, J. Zhu, Q. Zhang, J. Liu, Y. Jin, H. Wang, *ACS Appl. Mater. Interfaces* **2021**, *13*, 50319.
[21] J. Mandal, S. Du, M. Dontigny, K. Zaghib, N. Yu, Y. Yang, *Adv. Funct. Mater.* **2018**, *28*, 1802180.
[22] H. Zhao, Q. Sun, J. Zhou, X. Deng, J. Cui, *Adv. Mater.* **2020**, *32*, 2000870.
[23] S. Zeng, K. Shen, Y. Liu, A. P. Chooi, A. T. Smith, S. Zhai, Z. Chen, L. Sun, *Mater. Today* **2021**, *45*, 44.
[24] J. Li, X. Lu, Y. Zhang, X. Ke, X. Wen, F. Cheng, C. Wei, Y. Li, K. Yao, S. Yang, *Adv. Funct. Mater.* **2021**, *31*, 2102350.

[25] Q. Zhang, Y. Lv, Y. Wang, S. Yu, C. Li, R. Ma, Y. Chen, *Nat. Commun.* **2022**, *13*, 4874.
[26] X. Wang, X. Liu, Z. Li, H. Zhang, Z. Yang, H. Zhou, T. Fan, *Adv. Funct. Mater.* **2020**, *30*, 1907562.
[27] S. Wang, T. Jiang, Y. Meng, R. Yang, G. Tan, Y. Long, *Science* **2021**, *374*, 1501.
[28] Y. Tian, X. Liu, Z. Wang, J. Li, Y. Mu, S. Zhou, F. Chen, M. Minus, G. Xiao, Y. Zheng, *Nano Energy* **2022**, *96*, 107085.
[29] M. Zhu, T. Li, C. Davis, Y. Yao, J. Dai, Y. Wang, F. AlQatari, J. Gilman, L. Hu, *Nano Energy* **2016**, *26*, 332.
[30] Q. Liu, A. Frazier, X. Zhao, J. De La Cruz, A. Hess, R. Yang, I. Smalyukh, *Nano Energy* **2018**, *48*, 266.
[31] T. Li, M. Zhu, Z. Yang, J. Song, J. Dai, Y. Yao, W. Luo, G. Pastel, B. Yang, L. Hu, *Adv. Energy Mater.* **2016**, *6*, 1601122.
[32] P. Hsu, A. Song, P. Catrysse, C. Liu, Y. Peng, J. Xie, S. Fan, Y. Cui, *Science* **2016**, *353*, 1019.
[33] S. Zeng, S. Pian, M. Su, Z. Wang, M. Wu, X. Liu, M. Chen, Y. Xiang, J. Wu, M. Zhang, Q. Cen, Y. Tang, X. Zhou, Z. Huang, R. Wang, A. Tunuhe, X. Sun, Z. Xia, M. Tian, M. Chen, X. Ma, L. Yang, J. Zhou, H. Zhou, Q. Yang, X. Li, Y. Ma, G. Tao, *Science* **2021**, *373*, 692.
[34] P. Li, A. Wang, J. Fan, Q. Kang, P. Jiang, H. Bao, X. Huang, *Adv. Funct. Mater.* **2021**, 2109542.
[35] H. Qin, Y. Zhang, J. Jiang, L. Wang, M. Song, R. Bi, P. Zhu, F. Jiang, *Adv. Funct. Mater.* **2021**, 2106269.
[36] W. Yang, X. Li, X. Han, W. Zhang, Z. Wang, X. Ma, M. Li, C. Li, *Nano Energy* **2020**, *71*, 104610.
[37] B. Wicklein, A. Kocjan, G. Salazar-Alvarez, F. Carosio, G. Camino, M. Antonietti, L. Bergström, *Nat. Nanotechnol.* **2015**, *10*, 277.
[38] H. Zhang, X. Shen, E. Kim, M. Wang, J. H. Lee, H. Chen, G. Zhang, J. K. Kim, *Adv. Funct. Mater.* **2022**, *32*, 2111794.
[39] X. Ji, Y. Jiang, T. Liu, S. Lin, A. Du, *Cell Rep Phys Sci* **2022**, *3*, 100815.
[40] Z. Liu, J. Lyu, D. Fang, X. Zhang, *ACS Nano* **2019**, *13*, 5703.
[41] P. Hu, J. Wang, P. Zhang, F. Wu, Y. Cheng, J. Wang, Z. Sun, *Adv. Mater.* **2022**, 2207638.
[42] J. Wang, D. Liu, Q. Li, C. Chen, Z. Chen, P. Song, J. Hao, Y. Li, S. Fakhrhoseini, M. Naebe, X. Wang, W. Lei, *ACS Nano* **2019**, *13*, 7860.
[43] Y. Liu, Y. Zhang, T. Liao, L. Gao, M. Wang, X. Xu, X. Yang, H. Liu, *Carbohydr. Polym.* **2020**, *241*, 116425.
[44] J. Rostami, K. Gordeyeva, T. Benselfelt, E. Lahchaichi, S. A. Hall, A. V. Riazanova, P. A. Larsson, G. Ciftci, L. Wågberg, *Mater. Today* **2021**, *48*, 47.
[45] J. Erlandsson, T. Pettersson, T. Ingverud, H. Granberg, P. A. Larsson, M. Malkoch, L. Wagberg, *J. Mater. Chem. A* **2018**, *6*, 19371.
[46] H. Liu, T. Xu, C. Cai, K. Liu, W. Liu, M. Zhang, H. Du, C. Si, K. Zhang, *Adv. Funct. Mater.* **2022**, 2113082.
[47] Z. Zeng, E. Mavrona, D. Sacré, N. Kummer, J. Cao, L. A. E. Müller, E. Hack, P. Zolliker, G. Nyström, *ACS Nano* **2021**, *15*, 7451.
[48] Y. Chen, S. Li, X. Li, C. Mei, J. Zheng, S. E, G. Duan, K. Liu, S. Jiang, *ACS Nano* **2021**, *15*, 20666.
[49] Z. Zeng, C. Wang, G. Siqueira, D. Han, A. Huch, S. Abdolhosseinzadeh, J. Heier, F. Nüesch, C. Zhang, G. Nyström, *Adv. Sci.* **2020**, *7*, 2000979.
[50] X. Hu, J. Zhu, *Adv. Funct. Mater.* **2020**, *30*, 1907234.
[51] Z. Chen, H. Zhuo, Y. Hu, H. Lai, L. Liu, L. Zhong, X. Peng, *Adv. Funct. Mater.* **2020**, *30*, 1910292.
[52] M. Yang, Y. Shuai, K. S. Sunderland, C. Mao, *Adv. Funct. Mater.* **2017**, *27*, 1703726.
[53] G. Fu, X. Yan, Y. Chen, L. Xu, D. Sun, J. Lee, Y. Tang, *Adv. Mater.* **2018**, *30*, 1704609.
[54] R. Du, J. Joswig, R. Hgbner, L. Zhou, W. Wei, Y. Hu, A. Eychmgller, *Angew. Chem., Int. Ed.* **2020**, *59*, 8293.
[55] H. Liu, X. Chen, Y. Zheng, D. Zhang, Y. Zhao, C. Wang, C. Pan, C. Liu, C. Shen, *Adv. Funct. Mater.* **2021**, *31*, 2008006.
[56] F. Zhang, X. Lan, H. Peng, X. Hu, Q. Zhao, *Adv. Funct. Mater.* **2020**, *30*, 2002169.
[57] W. Xu, Y. Xing, J. Liu, H. Wu, Y. Cui, D. Li, D. Guo, C. Li, A. Liu, H. Bai, *ACS Nano* **2019**, *13*, 7930.
[58] P. Zhang, Q. Zhu, R. A. Soomro, S. He, N. Sun, N. Qiao, B. Xu, *Adv. Funct. Mater.* **2020**, *30*, 2000922.
[59] T. Benselfelt, J. Engström, L. Wågberg, *Green Chem.* **2018**, *20*, 2558.
[60] J. Erlandsson, T. Pettersson, T. Ingverud, H. Granberg, P. A. Larsson, M. Malkoch, L. Wagberg, *J. Mater. Chem. A* **2018**, *6*, 19371.
[61] H. Françon, Z. Wang, A. Marais, K. Mystek, A. Piper, H. Granberg, A. Malti, P. Gatenholm, P. A. Larsson, L. Wågberg, *Adv. Funct. Mater.* **2020**, *30*, 1909383.
[62] T. Benselfelt, L. Wågberg, *Biomacromolecules* **2019**, *20*, 2406.
[63] W. Tian, A. VahidMohammadi, M. S. Reid, Z. Wang, L. Ouyang, J. Erlandsson, T. Pettersson, L. Wågberg, M. Beidaghi, M. M. Hamedi, *Adv. Mater.* **2019**, *31*, 1902977.
[64] I. Usov, G. Nystro¨m, J. Adamcik, S. Handschin, C. Schu¨tz, A. Fall, L. Bergstro¨m, R. Mezzenga, *Nat. Commun.* **2015**, *6*, 7564.
[65] X. Han, S. Ding, L. Fan, Y. Zhou, S. Wang, *J. Mater. Chem. A* **2021**, *9*, 18614.
[66] Z. Hu, S. Yan, X. Li, R. You, Q. Zhang, D. L. Kaplan, *ACS Nano* **2021**, *15*, 8171.
[67] Q. Liu, J. Chen, T. Mei, X. He, W. Zhong, K. Liu, W. Wang, Y. Wang, M. Li, D. Wang, *J. Mater. Chem. A* **2018**, *6*, 3692.
[68] S. Zhao, Z. Zhang, G. Sèbe, R. Wu, R. V. Virtudazo, P. Tingaut, M. M. Koebel, *Adv. Funct. Mater.* **2015**, *25*, 2326.
[69] J. Shi, L. Lu, W. Guo, J. Zhang, Y. Cao, *Carbohydr. Polym.* **2013**, *98*, 282.
[70] C. Yue, J. Feng, J. Feng, Y. Jiang, *RSC Adv.* **2016**, *6*, 9396.
[71] Y. Kobayashi, T. Saito, A. Isogai, *Angew. Chem., Int. Ed.* **2014**, *53*, 10394.
[72] W. Huang, Y. Chen, Y. Luo, J. Mandal, W. Li, M. Chen, C. Tsai, Z. Shan, N. Yu, Y. Yang, *Adv. Funct. Mater.* **2021**, *31*, 2010334.
[73] M. Yang, W. Zou, J. Guo, Z. Qian, H. Luo, S. Yang, N. Zhao, L. Pattelli, J. Xu, D. S. Wiersma, *ACS Appl. Mater. Interfaces* **2020**, *12*, 25286.
[74] A. P. Raman, M. Anoma, L. Zhu, E. Rephaeli, S. Fan, *Nature* **2014**, *515*, 540.
[75] W. Gao, Z. Lei, K. Wu, Y. Chen, *Adv. Funct. Mater.* **2021**, *31*, 2100535.
[76] Z. Cheng, H. Han, F. Wang, Y. Yan, X. Shi, H. Liang, X. Zhang, Y. Shuai, *Nano Energy* **2021**, *89*, 106377.
[77] T. Wang, Y. Wu, L. Shi, X. Hu, M. Chen, L. Wu, *Nat. Commun.* **2021**, *12*, 365.
[78] L. Liu, X. Shan, X. Hu, W. Lv, J. Wang, *ACS Nano* **2021**, *15*, 19771.